

# Spin polarized electron-positron pair production via elliptical polarized laser fields

Anton Wöllert,<sup>\*</sup> Heiko Bauke,<sup>†</sup> and Christoph H. Keitel

Max-Planck-Institut für Kernphysik, Saupfercheckweg 1, 69117 Heidelberg, Germany

(Dated: June 25, 2015)

We study nonperturbative multiphoton electron-positron pair creation in ultrastrong electromagnetic fields formed by two counterpropagating pulses with elliptic polarization. Our numerical approach allows us to take into account the temporal as well as the spatial variation of the standing electromagnetic field. The spin and momentum resolved pair creation probabilities feature characteristic Rabi oscillations and resonance spectra. Therefore, each laser frequency features a specific momentum distribution of the created particles. We find that, depending on the relative polarization of both pulses, the created electrons may be spin polarized along the direction of field propagation.

PACS numbers: 12.20.Ds, 42.55.Vc, 42.50.Hz

## 1. Introduction

Quantum electrodynamics predicts the possible breakdown of the vacuum in the presence of ultrastrong electromagnetic fields into pairs of electrons and positrons. In the seminal articles by Sauter and others [1–3], pair creation was investigated theoretically for constant electromagnetic fields. Since then this process has been studied in numerous works; see Refs. [4, 5] for recent reviews. The Schwinger critical field strength of  $E_S = 1.3 \times 10^{18}$  V/m, where spontaneous pair creation is expected to set in, cannot be reached even by the strongest laser facilities available today. However, pair creation may be assisted by additional fields or particles or by electromagnetic fields that oscillate in time and space. Novel light sources envisage to provide field intensities in excess of  $10^{20}$  W/cm<sup>2</sup> and field frequencies in the x-ray domain [6–10]. The ELI-Ultra High Field Facility aims to reach intensities exceeding even  $10^{23}$  W/cm<sup>2</sup> corresponding to a field strength of about  $10^{15}$  V/m, which is only a few orders of magnitude below the critical field strength  $E_S$ . It has been argued that the intensity of such near-future ultrastrong light sources may be sufficient to observe pair creation [11–15].

Pair creation in laser fields is often studied by considering a time-varying homogeneous electric field [12, 13, 16–22]. Neglecting the magnetic field component and the spatial variation of the electric field eases the theoretical analysis and is motivated by the fact that a standing electromagnetic wave, which is formed by superimposing two counterpropagating linearly polarized waves of equal wavelength, intensity, and polarization, has a vanishing magnetic field component at positions, where the electric field reaches its maximum. A more realistic description of electron-positron pair creation, however, requires the consideration of inhomogeneous electric fields [23–27] or electromagnetic fields that depend on time and space [28–30].

Introducing the adiabaticity parameter  $\xi = eE/(m_0 c \omega)$  [21], where  $m_0$  denotes the electron mass,  $c$  the speed of light,  $e$  the elementary charge,  $E$  the peak electric field strength, and  $\omega$  the

electromagnetic field's angular frequency, one can distinguish two limiting cases of pair creation in oscillating electromagnetic fields [16] with frequencies  $\omega \lesssim m_0 c^2/\hbar$ . These two regimes are commonly referred to as nonperturbative Schwinger pair creation ( $\xi \gg 1$ ) and perturbative multiphoton pair creation ( $\xi \ll 1$ ). Note that these regimes are sometimes distinguished via the Keldysh parameter of vacuum pair creation  $\gamma$ , which is the inverse of  $\xi$ . In this contribution we will focus on the intermediate regime of nonperturbative multiphoton pair creation ( $\xi \approx 1$ ), which is most challenging from the theoretical point of view and, therefore, less well understood [21, 28, 31]. In particular, we consider pair creation in a standing electromagnetic wave formed by two counterpropagating waves. This means we include not only the electric field component but also the field's magnetic component, which can alter the pair creation rate [32, 33]. The temporal as well as spatial oscillations of these fields are accounted for. In our work the waves may have arbitrary elliptical polarization in contrast to prior publications where mainly linear polarization was considered. Electron dynamics in intense light with elliptical polarization [34] and pair creation via the nonlinear Bethe–Heitler process [35, 36] can show nontrivial spin effects [34, 35]. Therefore, pair creation in elliptically polarized light beams is expected to feature unexplored spin effects.

The manuscript is organized as follows. In Sec. 2 we describe the laser field configuration and pay special attention to the polarization of the light. We lay down the theoretical foundation for the numerical work in Sec. 3. The numerical methods are explained in Sec. 4. Our results are presented in Sec. 5. Typical Rabi oscillations of the pair creation probability and properties of the pair creation resonances are discussed. These resonance spectra are investigated for different polarizations and compared to a model that employs the dipole approximation, i. e., neglecting the magnetic field component and the spatial variation of the electric field. The dependence of pair creation on the final momenta of the created particles is discussed at the end of Sec. 5. Finally, we conclude in Sec. 6. For the reminder of this article, we will employ units with  $\hbar = 1$  and  $c = 1$ .

<sup>\*</sup> woellert@mpi-hd.mpg.de

<sup>†</sup> heiko.bauke@mpi-hd.mpg.de

## 2. Elliptically polarized light beams

In this work we will focus on a setup with two counterpropagating elliptically polarized laser beams with equal wavelength  $\lambda$ . Note that two counterpropagating laser beams with different wavelengths can always be transformed by a suitable Lorentz boost along the propagation direction into the considered setup. Furthermore, two crossed laser beams with the same wavelength and arbitrary but nonzero collision angle can always be transformed into the considered setup by a suitable Lorentz boost perpendicularly to the propagation direction. Similarly, two crossed laser beams with different wavelengths and arbitrary but nonzero collision angle can always be transformed by a suitable proper Lorentz transformation (which may include boosts as well as rotations) into the considered setup. Thus, it is quite generic.

Let us denote the unit vectors along the coordinate axes of the Cartesian coordinate system by  $\mathbf{e}_x$ ,  $\mathbf{e}_y$ , and  $\mathbf{e}_z$ . We assume that the two light beams propagate along the  $z$  direction, and thus their wave vectors equal  $\mathbf{k}_{\pm} = \pm k \mathbf{e}_z$  with  $k = 2\pi/\lambda$ . The indices distinguish beams traveling to the right (index “+”) and to the left (index “-”), respectively. To describe the polarization of an electromagnetic wave, it is convenient to use the Jones vector formalism [37]. The so-called Jones vectors  $|l\rangle$  and  $|r\rangle$  for circular polarized beams with left-handed and right-handed orientation are defined as

$$|l\rangle = \frac{1}{\sqrt{2}}(\mathbf{e}_x + i\mathbf{e}_y), \quad (1a)$$

$$|r\rangle = \frac{1}{\sqrt{2}}(\mathbf{e}_x - i\mathbf{e}_y). \quad (1b)$$

Any polarization state of the electric fields of the two laser beams can be formed by a linear combination of the Jones vectors  $|l\rangle$  and  $|r\rangle$ . At position  $\mathbf{r} = (x, y, z)$  and time  $t$ , the electric field of a single beam is given by

$$\mathbf{E}_{\pm}(\mathbf{r}, t) = \text{Re} \left( E \left( \cos \alpha_{\pm} |l\rangle + \sin \alpha_{\pm} e^{i\varphi_{\pm}} |r\rangle \right) e^{i(\pm kz - \omega t)} \right), \quad (2)$$

where  $\omega = k$  denotes the angular frequency and  $E$  the peak electric field strength. The expression (2) may be transformed into

$$\mathbf{E}_{\pm}(\mathbf{r}, t) = E \begin{pmatrix} \cos \varphi_{\pm}/2 & -\sin \varphi_{\pm}/2 \\ \sin \varphi_{\pm}/2 & \cos \varphi_{\pm}/2 \\ 0 & 0 \end{pmatrix} \times \begin{pmatrix} \cos(\pm kz - \omega t + \varphi_{\pm}/2) \cos(\alpha_{\pm} - \pi/4) \\ \sin(\pm kz - \omega t + \varphi_{\pm}/2) \sin(\alpha_{\pm} - \pi/4) \end{pmatrix}. \quad (3)$$

The second factor in (3) parametrizes an ellipse, and the parameters  $\alpha_{+}$  and  $\alpha_{-}$  determine its ellipticity. The parameters  $\varphi_{+}$  and  $\varphi_{-}$  specify the orientation of this ellipse via the first factor in (3), which represents a rotation matrix; see also Fig. 1. The light beams have linear polarization for  $\alpha_{\pm} = \pi/4$  and  $\alpha_{\pm} = 3\pi/4$ , while they have circular polarization for  $\alpha_{\pm} = 0$  and also for  $\alpha_{\pm} = \pi/2$ . The magnetic field component follows via  $\mathbf{B}_{\pm} = \mathbf{k}_{\pm} \times \mathbf{E}_{\pm}/k$ , and the mean intensity equals  $\varepsilon_0 E^2/2$  independent of  $\alpha_{\pm}$  and  $\varphi_{\pm}$ . The corresponding Coulomb-gauge

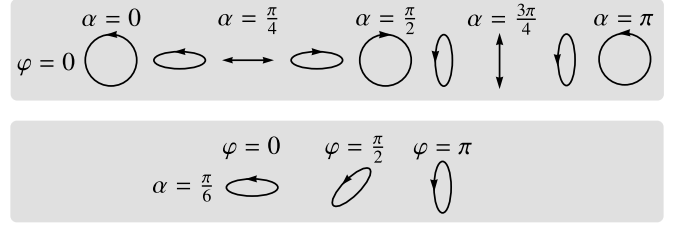


**FIG. 1:** (color online) Schematic illustration of different polarization states as a function of the parameters  $\alpha$  and  $\varphi$ , which determine the ellipticity (degree of polarization) and the orientation of the polarization ellipsis in the  $x$ - $y$  plane. Upper row for constant orientation  $\varphi$  but varying  $\alpha$ ; lower row for constant ellipticity  $\alpha$  but varying  $\varphi$ .

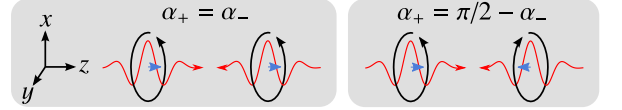


**FIG. 2:** (color online) Schematic illustration of the possible relative spin orientations of two counterpropagating electromagnetic fields. Left: When the fields' ellipticity parameters equal ( $\alpha_- = \alpha_+$ ), then both fields have the same sense of rotation. Consequently, also the superposition of both fields rotates around the  $z$  axis and this axis of rotation leads to a preferred direction along the positive or negative  $z$  axis. Right: For  $\alpha_- = \pi/2 - \alpha_+$  the sense of rotation is exactly opposite. Thus, the resulting field does not rotate, and no direction of the  $z$  axis is preferred.

vector potential is

$$\mathbf{A}_{\pm}(\mathbf{r}, t) = \text{Re} \left( \frac{E}{i\omega} \left( \cos \alpha_{\pm} |l\rangle + \sin \alpha_{\pm} e^{i\varphi_{\pm}} |r\rangle \right) e^{i(\pm kz - \omega t)} \right) \quad (4)$$

or equivalently

$$\mathbf{A}_{\pm}(\mathbf{r}, t) = \frac{E}{\omega} \begin{pmatrix} \cos \varphi_{\pm}/2 & -\sin \varphi_{\pm}/2 \\ \sin \varphi_{\pm}/2 & \cos \varphi_{\pm}/2 \\ 0 & 0 \end{pmatrix} \times \begin{pmatrix} \sin(\pm kz - \omega t + \varphi_{\pm}/2) \cos(\alpha_{\pm} - \pi/4) \\ -\cos(\pm kz - \omega t + \varphi_{\pm}/2) \sin(\alpha_{\pm} - \pi/4) \end{pmatrix}. \quad (5)$$

The total vector potential of two counterpropagating electromagnetic waves equals  $\mathbf{A} = \mathbf{A}_{+} + \mathbf{A}_{-}$  and similarly for the electric and magnetic field components. In the reminder of this article, we will assume that both counterpropagating light waves have the same orientation, i. e.,  $\varphi_{+} = \varphi_{-}$ , and that they have the same ellipticity, i. e.,  $\alpha_{-} = \alpha_{+}$  or  $\alpha_{-} = \pi/2 - \alpha_{+}$  depending on the sense of rotation being identical or opposite to each other; see Fig. 2. Note that for any such field configuration we can always find a coordinate system by a rotation around the  $z$  axis, where  $\varphi_{+} = \varphi_{-} = 0$ . Thus, we will set in the following  $\varphi_{+} = \varphi_{-} = 0$  without loss of generality.

Elliptically polarized light beams carry photonic spin angular momentum [38], which is  $\varepsilon_0 E^2 \cos(2\alpha_{\pm})/(\omega)$  for each of the two considered counterpropagating light beams. Thus, the ellipticity parameters  $\alpha_{+}$  and  $\alpha_{-}$  determine the photonic spin density. The total spin density of the considered setup equals  $2\varepsilon_0 E^2 \cos(2\alpha_{\pm})/\omega$  (with orientation along the  $z$  direction) for

the case that both individual beams have the opposite helicity, i. e.,  $\alpha_+ = \alpha_-$ ; see also the left part of Fig. 2. The total photonic spin density vanishes if both light beams have same helicity, i. e.,  $\alpha_+ = \pi/2 - \alpha_-$ ; see also the right part of Fig. 2. In what follows, we will name the field setup “corotating” if  $\alpha_+ = \alpha_-$  and “antirrotating” if  $\alpha_+ = \pi/2 - \alpha_-$ .

### 3. Theoretical foundations

Quantum electrodynamics has to be applied to describe pair creation in electromagnetic fields [39]. The Hamiltonian describing the dynamics of a quantum field state in an external electromagnetic field is given by

$$\hat{H}(t) = \int \hat{\psi}(\mathbf{r})^\dagger \mathcal{H}(t) \hat{\psi}(\mathbf{r}) d^3r, \quad (6)$$

where  $\hat{\psi}(\mathbf{r})$  denotes the time-independent spinor field operator and

$$\mathcal{H}(t) = \boldsymbol{\alpha} \cdot (-i\nabla - q\mathbf{A}(\mathbf{r}, t)) + m_0\beta \quad (7)$$

is the Dirac Hamiltonian for a particle with charge  $q$  and rest mass  $m_0$ . Furthermore,  $\boldsymbol{\alpha} = (\alpha_x, \alpha_y, \alpha_z)^\top$  and  $\beta$  stand for the Dirac matrices [40, 41]. Let us denote the times, when the interaction with the external electromagnetic field sets in and ends, by  $t_{\text{in}}$  and  $t_{\text{out}}$ , respectively. Thus,  $\mathbf{E}(t) = 0$  for  $t \leq t_{\text{in}}$ , and for  $t \geq t_{\text{out}}$ . The Dirac Hamiltonian may be diagonalized at times  $t_{\text{in}}$  and  $t_{\text{out}}$  by introducing the two complete sets of orthonormal functions  ${}_{\pm}\varphi_n(\mathbf{r})$  and  ${}^{\pm}\varphi_n(\mathbf{r})$  [42],

$$\mathcal{H}(t_{\text{in}}){}_{\pm}\varphi_n(\mathbf{r}) = {}_{\pm}\varepsilon_n {}_{\pm}\varphi_n(\mathbf{r}), \quad (8a)$$

$$\mathcal{H}(t_{\text{out}}){}^{\pm}\varphi_n(\mathbf{r}) = {}^{\pm}\varepsilon_n {}^{\pm}\varphi_n(\mathbf{r}), \quad (8b)$$

where  ${}_{+}\varepsilon_n > 0$ ,  ${}_{-}\varepsilon_n < 0$  and  ${}^{+}\varepsilon_n > 0$ ,  ${}^{-}\varepsilon_n < 0$  denote the corresponding positive and negative eigenenergies, with  $n$  labeling the quantum state. Then the spinor field operator  $\hat{\psi}(\mathbf{r})$  may be decomposed in one of the two bases

$$\hat{\psi}(\mathbf{r}) = \sum_n {}_{+}\varphi_n(\mathbf{r}) \hat{a}_n(t_{\text{in}}) + {}_{-}\varphi_n(\mathbf{r}) \hat{b}_n^\dagger(t_{\text{in}}), \quad (9a)$$

$$\hat{\psi}(\mathbf{r}) = \sum_n {}^{+}\varphi_n(\mathbf{r}) \hat{a}_n(t_{\text{out}}) + {}^{-}\varphi_n(\mathbf{r}) \hat{b}_n^\dagger(t_{\text{out}}), \quad (9b)$$

where  $\hat{a}^\dagger$ ,  $\hat{a}$  and  $\hat{b}^\dagger$ ,  $\hat{b}$ , denote the creation and the annihilation operators for the electron and the positron, respectively, at times  $t_{\text{in}}$  and  $t_{\text{out}}$ . Quantum field states before and after interaction with definite numbers of particles can always be written as products of the vacuum states  $|0, t_{\text{in}}\rangle$  and  $|0, t_{\text{out}}\rangle$  and a number of particle and antiparticle creation operators,

$$|t_{\text{in}}\rangle = \hat{a}_{n_1}^\dagger(t_{\text{in}}) \hat{a}_{n_2}^\dagger(t_{\text{in}}) \dots \hat{b}_{m_1}^\dagger(t_{\text{in}}) \hat{b}_{m_2}^\dagger(t_{\text{in}}) \dots |0, t_{\text{in}}\rangle, \quad (10a)$$

$$|t_{\text{out}}\rangle = \hat{a}_{n_1}^\dagger(t_{\text{out}}) \hat{a}_{n_2}^\dagger(t_{\text{out}}) \dots \hat{b}_{m_1}^\dagger(t_{\text{out}}) \hat{b}_{m_2}^\dagger(t_{\text{out}}) \dots |0, t_{\text{out}}\rangle. \quad (10b)$$

The amplitude for the transition between these states is given by

$$M_{\text{in} \rightarrow \text{out}} = \langle t_{\text{out}} | \hat{U}(t_{\text{out}}, t_{\text{in}}) | t_{\text{in}} \rangle, \quad (11)$$

where  $\hat{U}(t_{\text{out}}, t_{\text{in}})$  denotes the time evolution operator that corresponds to the Hamiltonian  $\hat{H}(t)$  and maps the state  $|t_{\text{in}}\rangle$  at time  $t_{\text{in}}$  to some later time  $t_{\text{out}}$ .

After interaction the average number of electrons in quantum state  $n$  is given by

$$\mathcal{N}_n = \langle \hat{U}(t_{\text{out}}, t_{\text{in}}) t_{\text{in}} | \hat{a}_n^\dagger(t_{\text{out}}) \hat{a}_n(t_{\text{out}}) | \hat{U}(t_{\text{out}}, t_{\text{in}}) t_{\text{in}} \rangle \quad (12)$$

or equivalently

$$\mathcal{N}_n = \langle t_{\text{in}} | \hat{a}_n^\dagger(t_{\text{out}}) \hat{a}_n(t_{\text{out}}) | t_{\text{in}} \rangle, \quad (13)$$

where

$$\hat{a}_n(t_{\text{out}}) = \hat{U}(t_{\text{out}}, t_{\text{in}})^\dagger \hat{a}_n(t_{\text{out}}) \hat{U}(t_{\text{out}}, t_{\text{in}}) \quad (14)$$

is the representation of the electron creation operator in the Heisenberg picture with  $|t_{\text{in}}\rangle$  as the reference state. In the Heisenberg picture, the spinor field operator  $\hat{\psi}(\mathbf{r})$  is replaced by the time-dependent operator  $\hat{\psi}(\mathbf{r}, t)$  of which the evolution is determined by the Dirac equation

$$i\hat{\psi}(\mathbf{r}, t) = \mathcal{H}(t)\hat{\psi}(\mathbf{r}, t). \quad (15)$$

At time  $t_{\text{in}}$  the operator  $\hat{\psi}(\mathbf{r}, t)$  equals (9a), and at later times

$$\hat{\psi}(\mathbf{r}, t) = \hat{U}(t, t_{\text{in}})^\dagger \hat{\psi}(\mathbf{r}) \hat{U}(t, t_{\text{in}}) \quad (16)$$

or equivalently

$$\hat{\psi}(\mathbf{r}, t) = \int G(\mathbf{r}, t_{\text{out}}; \mathbf{r}', t_{\text{in}}) \hat{\psi}(\mathbf{r}') d^3r', \quad (17)$$

where  $G(\mathbf{r}, t; \mathbf{r}', t')$  denotes the complete Green function of (15). Using

$$\hat{a}_n(t_{\text{out}}) = \int {}^{+}\varphi_n(\mathbf{r})^\dagger \hat{\psi}(\mathbf{r}, t) d^3r, \quad (18)$$

(9a), and (17), we get

$$\hat{a}_n(t_{\text{out}}) = \sum_m G({}^{+}|_{+})_{n;m} \hat{a}_m(t_{\text{in}}) + G({}^{+}|_{-})_{n;m} \hat{b}_m^\dagger(t_{\text{in}}) \quad (19)$$

with  $G({}^{\pm}|_{\pm})_{n;m}$  defined as

$$G({}^{\pm}|_{\pm})_{n;m} = {}^{\pm}\varphi_n(\mathbf{r})^\dagger G(\mathbf{r}, t_{\text{out}}; \mathbf{r}', t_{\text{in}}) {}_{\pm}\varphi_m(\mathbf{r}') d^3r' d^3r. \quad (20)$$

Choosing the vacuum state  $|0, t_{\text{in}}\rangle$  as the initial state  $|t_{\text{in}}\rangle$ , one can show with (19) that [43]

$$\mathcal{N}_n = \sum_m G({}^{+}|_{-})_{n;m}^* G({}^{+}|_{-})_{n;m} = \sum_m |G({}^{+}|_{-})_{n;m}|^2, \quad (21)$$

and therefore the expectation value of the total number of created electrons is

$$\mathcal{N} = \sum_{m,n} |G({}^{+}|_{-})_{n;m}|^2. \quad (22)$$

Note that the quantity  $|G({}^{+}|_{-})_{n;m}|^2$  denotes the probability that a negative-energy state with the quantum number  $m$  turns into a positive-energy state with the quantum number  $n$ . A similar calculation yields the expectation value of the total number of created positrons  $\sum_{m,n} |G({}^{-}|_{+})_{n;m}|^2$ . In order to keep the manuscript compact, we will present results for the created electrons only. Due to the symmetry of the pair creation process, corresponding results for the positron can be deduced from calculations for the electron.

## 4. Numerical solution of the Dirac equation in monochromatic fields

In Sec. 3 we outlined that the number of created pairs can be determined via the quantities  $G(\pm|_{\pm})_{n,m}$ , which can also be written as

$$G(\pm|_{\pm})_{n,m} = \int \pm \varphi_n(\mathbf{r})^\dagger \pm \varphi_m(\mathbf{r}, t_{\text{out}}) d^3r, \quad (23)$$

where  $\pm \varphi_m(\mathbf{r}, t)$  is a solution of the time-dependent Dirac equation (15) with the initial condition  $\pm \varphi_m(\mathbf{r}, t_{\text{in}}) = \pm \varphi_m(\mathbf{r})$ . Thus, we can analyze the quantum electrodynamical problem of pair creation by solving a large number of independent time-dependent single-particle problems for the Dirac equation (15). For the setup of Sec. 2, it is appropriate to solve these in momentum space. The (real-valued) total vector potential  $\mathbf{A} = \mathbf{A}_+ + \mathbf{A}_-$  can always be written in the form

$$\mathbf{A}(\mathbf{r}, t) = \mathbf{a}(t)e^{-ikz} + \mathbf{a}(t)^*e^{ikz} \quad (24)$$

with some complex-valued vector  $\mathbf{a}(t)$  and its conjugate  $\mathbf{a}(t)^*$ . Because the external laser field was assumed to be monochromatic, the operator  $\boldsymbol{\alpha} \cdot \mathbf{A}$  (and consequently also the Dirac Hamiltonian) couples momentum eigenstates with momentum  $\mathbf{p}$  only to momentum eigenstates with momentum  $\mathbf{p} \pm k\mathbf{e}_z$ , which simplifies the numerical treatment considerably. Because of the monochromatic field (24), the Hilbert space separates into disjunct subspaces, and each of them is spanned by plane waves with momentum  $n\mathbf{k}\mathbf{e}_z + \mathbf{p}_0$  with integer  $n$ , where the base momentum  $\mathbf{p}_0$  selects a specific subspace. To take advantage of this symmetry, we expand the single-particle wave functions into plane waves as

$$\Psi(\mathbf{r}, t) = \sum_{n,\gamma} d_n^\gamma(t) \sqrt{\frac{k}{2\pi}} \psi^\gamma e^{i(n\mathbf{k}\mathbf{e}_z + \mathbf{p}_0) \cdot \mathbf{r}} \quad (25)$$

with  $\gamma \in \{1, 2, 3, 4\}$  and the vectors

$$\psi^1 = (1, 0, 0, 0)^\top, \quad (26a)$$

$$\psi^2 = (0, 1, 0, 0)^\top, \quad (26b)$$

$$\psi^3 = (0, 0, 1, 0)^\top, \quad (26c)$$

$$\psi^4 = (0, 0, 0, 1)^\top. \quad (26d)$$

The expansion (25) into a *discrete* set of plane waves would also be justified for multicolor setups provided that all wave vectors are an integer multiple of  $k\mathbf{e}_z$ . Defining

$$d_n(t) = (d_n^1(t), d_n^2(t), d_n^3(t), d_n^4(t))^\top \quad (27)$$

and using the expansion (25), the Dirac equation reads

$$i\dot{d}_n(t) = (\boldsymbol{\alpha} \cdot (n\mathbf{k}\mathbf{e}_z + \mathbf{p}_0) + \beta m_0)d_n(t) - w(t)q\boldsymbol{\alpha} \cdot \mathbf{a}(t)d_{n-1}(t) - w(t)q\boldsymbol{\alpha} \cdot \mathbf{a}(t)^*d_{n+1}(t) \quad (28)$$

in momentum space. Here, the window function

$$w(t) = \begin{cases} \sin^2 \frac{\pi(\Delta T - t)}{2\Delta T} & \text{if } -\Delta T \leq t \leq 0, \\ 1 & \text{if } 0 \leq t \leq T, \\ \sin^2 \frac{\pi(T + \Delta T - t)}{2\Delta T} & \text{if } T \leq t \leq T + \Delta T, \end{cases} \quad (29)$$

has been introduced to model a smooth turn on and turn off of the external laser field at  $t = t_{\text{in}} = -\Delta T$  and  $t = t_{\text{out}} = T + \Delta T$ .

As the vector potential vanishes at  $t_{\text{in}}$  and  $t_{\text{out}}$ , the states  $\pm \varphi_n(\mathbf{r})$  and  $\pm \varphi_n(\mathbf{r})$  are free-particle states with definite momentum, energy, and spin orientation (in the  $z$  direction), which read explicitly

$$+\varphi_{n,\uparrow/\downarrow}(\mathbf{r}) = +\varphi_{n,\uparrow/\downarrow}(\mathbf{r}) = u_{n\mathbf{k}\mathbf{e}_z + \mathbf{p}_0, \uparrow/\downarrow} e^{i(n\mathbf{k}\mathbf{e}_z + \mathbf{p}_0) \cdot \mathbf{r}}, \quad (30a)$$

$$-\varphi_{n,\uparrow/\downarrow}(\mathbf{r}) = -\varphi_{n,\uparrow/\downarrow}(\mathbf{r}) = v_{n\mathbf{k}\mathbf{e}_z + \mathbf{p}_0, \uparrow/\downarrow} e^{i(n\mathbf{k}\mathbf{e}_z + \mathbf{p}_0) \cdot \mathbf{r}}, \quad (30b)$$

where we have replaced the generic quantum number  $n$  by the quantum numbers  $(n, \uparrow)$  or  $(n, \downarrow)$ , which specify the particle's momentum ( $n\mathbf{k}\mathbf{e}_z + \mathbf{p}_0$ ) and its spin state (up or down). We also introduced

$$u_{\mathbf{p}, \uparrow/\downarrow} = \sqrt{\frac{m_0 + \mathcal{E}(\mathbf{p})}{2\mathcal{E}(\mathbf{p})}} \begin{pmatrix} \chi_{\uparrow/\downarrow} \\ \frac{\boldsymbol{\sigma} \cdot \mathbf{p}}{m_0 + \mathcal{E}(\mathbf{p})} \chi_{\uparrow/\downarrow} \end{pmatrix}, \quad (31a)$$

$$v_{\mathbf{p}, \uparrow/\downarrow} = \sqrt{\frac{m_0 + \mathcal{E}(\mathbf{p})}{2\mathcal{E}(\mathbf{p})}} \begin{pmatrix} -\frac{\boldsymbol{\sigma} \cdot \mathbf{p}}{m_0 + \mathcal{E}(\mathbf{p})} \chi_{\uparrow/\downarrow} \\ \chi_{\uparrow/\downarrow} \end{pmatrix} \quad (31b)$$

with  $\chi_\uparrow = (1, 0)^\top$  and  $\chi_\downarrow = (0, 1)^\top$  and  $\mathcal{E}(\mathbf{p}) = \sqrt{m_0^2 + \mathbf{p}^2}$ . In Fourier space the states  $+\varphi_{n,\uparrow/\downarrow}(\mathbf{r})$  and  $+\varphi_{n,\uparrow/\downarrow}(\mathbf{r})$  correspond to

$$d_l = \begin{cases} u_{n\mathbf{k}\mathbf{e}_z + \mathbf{p}_0, \uparrow/\downarrow} & \text{for } l = n \\ (0, 0, 0, 0)^\top & \text{else,} \end{cases} \quad (32a)$$

while  $-\varphi_{n,\uparrow/\downarrow}(\mathbf{r})$  and  $-\varphi_{n,\uparrow/\downarrow}(\mathbf{r})$  correspond to

$$d_l = \begin{cases} v_{n\mathbf{k}\mathbf{e}_z + \mathbf{p}_0, \uparrow/\downarrow} & \text{for } l = n \\ (0, 0, 0, 0)^\top & \text{else.} \end{cases} \quad (32b)$$

Choosing  $-\varphi_{m,\uparrow}(\mathbf{r})$  as the initial state at  $t = t_{\text{in}} = -\Delta T$ , the desired transition matrix element for transitions from the negative-energy state  $(m, \uparrow)$  to the positive-energy state  $(n, \uparrow)$  reads in terms of the Fourier space coefficients

$$G(+|-)_{n,\uparrow;m,\uparrow} = u_{n\mathbf{k}\mathbf{e}_z + \mathbf{p}_0, \uparrow}^\dagger d_m(T) \quad (33)$$

and analogously for other transitions. The average number of created electrons with momentum  $n\mathbf{k}\mathbf{e}_z + \mathbf{p}_0$  and spin up/down is given by

$$\mathcal{N}_{n,\uparrow/\downarrow} = \sum_m |G(+|-)_{n,\uparrow/\downarrow;m,\uparrow}|^2 + |G(+|-)_{n,\uparrow/\downarrow;m,\downarrow}|^2. \quad (34)$$

Thus, the spin-resolved average total number of created electrons becomes

$$\mathcal{N}_{\uparrow/\downarrow} = \sum_n \mathcal{N}_{n,\uparrow/\downarrow}, \quad (35)$$

and the average total number of created electrons equals

$$\mathcal{N} = \mathcal{N}_\uparrow + \mathcal{N}_\downarrow. \quad (36)$$

The Dirac equation in momentum space (28) is an infinite system of ordinary differential equations. In a numerical solution, however, we have to limit the system to a finite number of modes. This is justified because the interaction term



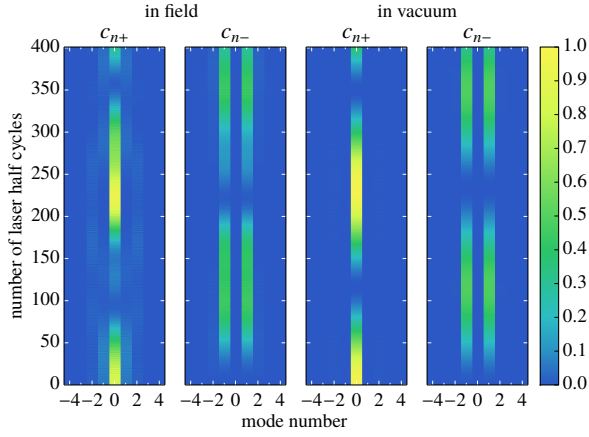


**FIG. 3:** (color online) Time evolution of the initial momentum eigenstate  $u_{p=0,\uparrow}$  and its spreading into neighboring positive and negative momentum eigenstates for  $\alpha_- = \alpha_+ = \pi/4$ ,  $\omega = 0.472 m_0$  and  $\xi = 1/2$ . The vertical axis specifies the interaction time with the external field, and the horizontal axis specifies the momentum mode  $\mathbf{p} = n\mathbf{k}\mathbf{e}_z + 0$ . In field: The propagated state is decomposed into free momentum eigenstates without turning off the laser field. This is not unambiguous for physical interpretation. In vacuum: The external field has been turned off smoothly before decomposing the propagated wave function, allowing for a physical interpretation as momentum eigenstates.

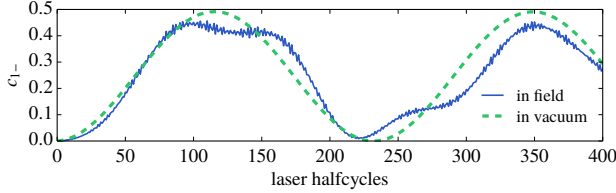


**FIG. 4:** (color online) More detailed plot of the difference between taking an expectation value, while the electromagnetic field is still acting (in field) or has been smoothly turned off (in vacuum). Both lines correspond to the plotted weights  $c_{n-}$  (38b) of Fig. 3 with mode number 1. Taking the expectation values in the field leads to no unique physical identification and also shows faster oscillations on the order of the laser frequency  $\omega$ . In contrast, a measurement after the field has been turned off yields a clear and smooth Rabi oscillation with respect to the interaction time with the external laser.

$w(t)q\mathbf{a} \cdot \mathbf{a}(t)$  does not depend on the mode number  $n$ , but the free Dirac Hamiltonian grows asymptotically linearly with  $n$ . Thus, for large  $n$  transitions between different free-particle states are suppressed, and consequently large- $n$  states do not contribute to pair creation. The system of ordinary differential equations (28) is solved via a Fourier split operator method similar to the method presented in Ref. [44].

## 5. Numerical results

### 5.1. Single-mode dynamics

To help the reader understanding the following simulations, we would like to start with an example of a single time evolution. Both lasers are set up with linear polarization, i. e.,  $\alpha_- = \alpha_+ = \pi/4$ , and  $\xi = 1/2$ , where  $\xi$  is determined with respect to a single laser field. Taking into account the electromagnetic fields of both lasers would yield larger values of  $\xi$ , in particular  $\xi = 1$  in case of linear polarization. To calculate the expectation value of an electron being created with zero momentum and spin up, the initial state must be set to  $u_{p=0,\uparrow}$ ; see Eq. (31a). Now, according to Eq. (21), the propagation back in time needs to be calculated. The duration of the external electromagnetic field can be varied and will be given by the number of half-cycles of the lasers period

$$T = (\text{number of half-cycles}) \times \frac{\pi}{\omega}. \quad (37)$$

During this evolution (including the turn on [45]), the initially localized wave function spreads in momentum space to neighboring “modes” with momentum  $\mathbf{p} = n\mathbf{k}\mathbf{e}_z + \mathbf{p}_0$ . Furthermore, the wave function will also start to occupy negative energy modes  $v_{p,\uparrow/\downarrow}$ . Let  $\varphi(t)$  be the propagated wave function; then

$$c_{n+}(t) = |\langle u_{p,\uparrow} | \varphi(t) \rangle|^2 + |\langle u_{p,\downarrow} | \varphi(t) \rangle|^2, \quad (38a)$$

$$c_{n-}(t) = |\langle v_{p,\uparrow} | \varphi(t) \rangle|^2 + |\langle v_{p,\downarrow} | \varphi(t) \rangle|^2 \quad (38b)$$

define the weights (probability coefficients) of this wave function to be in a positive ( $c_{n+}$ ) or negative ( $c_{n-}$ ) energy mode with momentum  $\mathbf{p} = n\mathbf{k}\mathbf{e}_z + \mathbf{p}_0$ . Here, the spin degree of freedom has already been summed out. This decomposition into free momentum eigenstates is not suited for physical interpretation [21] if the external field is still acting, because the free momentum eigenstates do not represent eigenstates of the Dirac Hamiltonian in the presence of an external electromagnetic field. Hence, for a unique physical interpretation, the external field is turned off smoothly, and then the decomposition into free momentum eigenstates is carried out. Both cases, with and without turn off, are shown in Fig. 3. They look quite the same for this set of parameters, but indeed they are different. This difference is visualized in more detail in Fig. 4 for the weight  $c_{n-}$  with mode number  $n = 1$ . The measurement in the field contains oscillation noise with frequencies on the order of the laser frequency. These unphysical oscillations vanish, if the measurement is performed in a properly switched-off field. For the measurement in vacuum, all plots in Figs. 3 and 4 show a slow oscillation with respect to the duration of the electromagnetic field, corresponding to a Rabi oscillation of  $N_{0,\uparrow}$ , which is the expectation value for the creation of an electron with zero momentum and spin up, given by the sum over all weights  $c_{n-}$  in the negative-energy subspace. Similar Rabi oscillations have been predicted for the relativistic Kapitza–Dirac effect [46, 47].

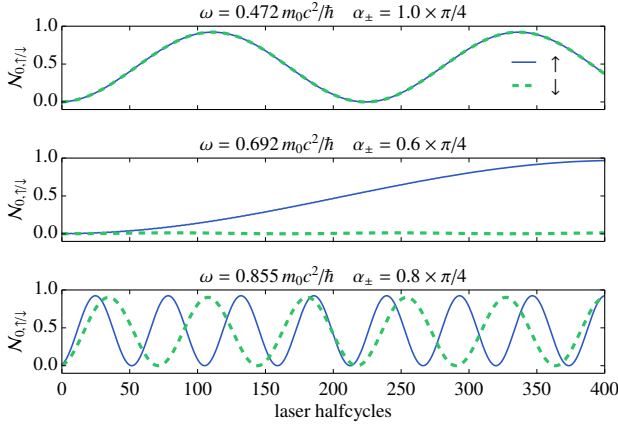


**FIG. 5:** (color online) Rabi oscillations for the average occupation number  $N_{0,\uparrow/\downarrow}$  of electrons with final momentum  $\mathbf{p} = 0$ . Three different parameter sets for the polarization parameters  $\alpha_-$  and  $\alpha_+$  have been chosen, while  $\xi = 1/2$  is kept for all. Top: The clearly visible resonant Rabi oscillation is independent of the final spin orientation due to the linear polarization. Middle: Only the electron with spin up is at resonance for this specific elliptical polarization set, while the electron with spin down is completely off resonant. Bottom: Both spin orientations are slightly off resonant with almost the same oscillation amplitude but different Rabi frequencies.

## 5.2. Rabi oscillations

It was mentioned in the previous subsection that the expectation values for creating electrons and positrons with specific momentum and spin (given by the occupation number (34)) will exhibit Rabi-type oscillations with respect to the interaction time in the external field. Choosing a particular set of values for the polarization parameters  $\alpha_+$  and  $\alpha_-$ , the field strength (determined via  $\xi$ ), and the final momenta and spin ( $\mathbf{p}, \uparrow/\downarrow$ ) for the created particles of interest, pair creation becomes resonant for specific frequencies of the laser field. Three distinctive parameter sets are shown in Fig. 5. For all plots, the parameter  $\xi$  equals  $1/2$ , and the final momenta of interest for the created electron is set to  $\mathbf{p} = 0$ . The upper plot shows that the resonance of the average number of created electrons is independent on their final spin in a laser setup with linear polarization. For  $\alpha_+ = \alpha_- = 0.6 \times \pi/4$ , however, a spin effect can be observed as illustrated in the middle part of Fig. 5. The created electron with spin up is at resonance, while the electron with spin down is clearly off resonant and does not show any noticeable Rabi oscillation. The bottom plot shows that for an elliptical polarization ( $\alpha_+ = \alpha_- = 0.8 \times \pi/4$ , not far from linear polarization) both Rabi oscillations of the two possible spin orientations are slightly off resonant and almost equal in their amplitude, but their Rabi frequencies differ.

## 5.3. Resonance spectra

In this and the following two sections, we will consider particles having zero momentum only, while Sec. 5.6 will allow for the case of nonzero momentum. Having examined the Rabi

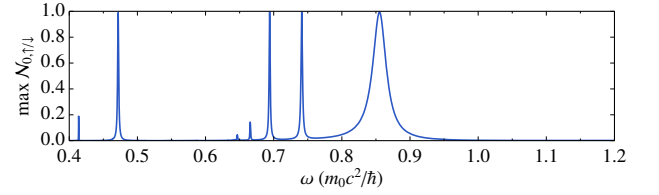


**FIG. 6:** (color online) Pair production resonances for linear polarization  $\alpha_- = \alpha_+ = \pi/4$  and  $\xi = 1/2$ . For each laser frequency  $\omega$ , a simulation of the type in Sec. 5.2 is performed, and the maximum value of  $N_{0,\uparrow/\downarrow}$  is taken as the ordinate value for this frequency. The spin of the produced electron needs not be distinguished for electrons with zero momentum due to the linear polarization. Four distinct resonance peaks can be seen with increasing resonance width as the laser frequency increases. The smaller peaks have a very low Rabi frequency and do not reach a full Rabi cycle as the maximum interaction time of this simulation is limited to 401 half-cycles of the laser field. For longer interaction times, these resonance peaks will grow, and new ones may emerge.

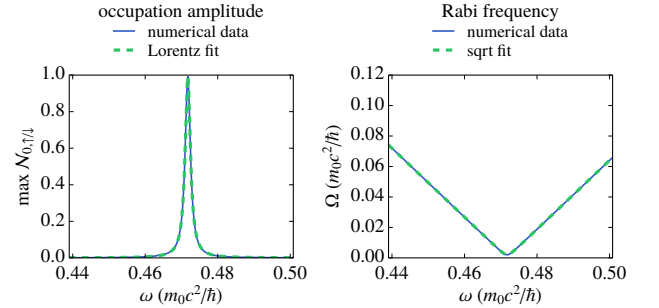


**FIG. 7:** (color online) Resonance at  $\omega \approx 0.472 m_0$  for linearly polarized waves with  $\alpha_+ = \alpha_- = \pi/4$  and  $\xi = 1/2$  in detail. Left: The pair production amplitude resonance including a Lorentz fit (39) for the resonance peak. Right: The Rabi oscillation frequency  $\Omega$  and its dependence on the detuning, including a fit of the form (40). Both fits agree perfectly well. The numerical fit values for the Lorentz fit are  $\omega_R = 0.47174(1) m_0$  and  $w = 0.001780(3) m_0$ , and a fit to (40) yields  $\Omega_R = 0.002012(4) m_0$ ,  $\eta = 2.26639(4)$ , and  $\omega_R = 0.47175(1) m_0$ .

oscillations for specific laser frequencies, we will analyze the pair-creation spectra now. Each data point of a pair-creation spectrum represents the maximum value of  $N_{0,\uparrow/\downarrow}$  for a specific set of laser parameters. Figure 6 shows the maximum value of  $N_{0,\uparrow/\downarrow}$  as a function of the laser frequency  $\omega$  while keeping all other parameters fixed. Here the polarization is linear, i. e.,  $\alpha_- = \alpha_+ = \pi/4$ , and  $\xi = 1/2$ . Note that in case of linear polarization pair-creation probabilities do not depend on the spin orientation, and therefore  $N_{0,\uparrow} = N_{0,\downarrow}$ . Four complete resonances can be inferred from Fig. 6. Their resonance width increases with increasing frequency. Furthermore, three smaller resonances appear that do not reach the full resonance maximum of unity. The reason for this is that their Rabi oscillation frequencies are very low and the top of the Rabi cycle has not been reached before the simulation ends as the maximum interaction time with the external field has been limited to 401 half-cycles of the external laser field for this simulation.

A close-up sweep of the resonance at  $\omega \sim 0.472 m_0$  has been

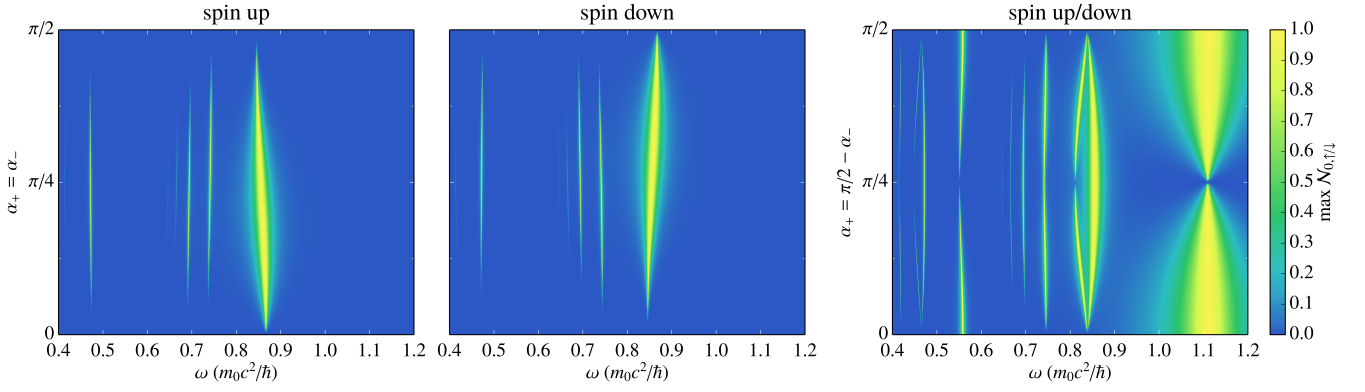


**FIG. 8:** (color online) Polarization and laser frequency dependence of the electron creation probability with zero final momentum and specific spin orientation with respect to the positive  $z$  direction. Both lasers field strengths' are determined by their frequency  $\omega$  and  $\xi = 1/2$ . The color encodes the maximum electron creation probability measured for a time of maximum 400 half-cycles of the laser fields period. Various resonances can be seen, which change their resonance frequency  $\omega_R$  with varying ellipticity  $\alpha_{\pm}$ . Left two plots: Both plots correspond to the case of corotating laser fields. A slice along the line of linear polarization  $\alpha_+ = \pi/4$  would correspond to the spectrum Fig. 6. Except for  $\alpha_+ = \pi/4$ , which corresponds to linear polarization, electron creation probabilities depend on the spin orientation of the created electron. Note that pair creation is completely suppressed for circular polarized light ( $\alpha_{\pm} = 0$  or  $\alpha_{\pm} = \pi/2$ ). Right plot: This represents the resonance spectra for antirotating fields, where the electron creation probabilities do not depend on the spin orientation.

done to show the typical Rabi characteristics. One characteristic, the Lorentz type resonance shape, is plotted on the left of Fig. 7 with a fit to the Lorentz function

$$\max \mathcal{N}_{0,\uparrow/\downarrow} = \frac{1}{1 + \left(\frac{\omega - \omega_R}{w/2}\right)^2}. \quad (39)$$

The fit parameter  $\omega_R$  corresponds to the resonance frequency, and  $w$  gives to the full width at half maximum. Furthermore, the Rabi oscillation frequency  $\Omega$  can be extracted from the numerical data for each laser frequency  $\omega$ . The right part of Fig. 7 shows the Rabi frequency  $\Omega$  together with a fit to the function

$$\Omega = \sqrt{\Omega_R^2 + \eta^2(\omega - \omega_R)^2}, \quad (40)$$

where  $\Omega_R$  denotes the Rabi frequency at resonance and  $\eta$  is a fit coefficient depending on the resonance. It can be seen that both fits agree perfectly well with the numerical data and hence justify the categorization of pair production in this parameter regime as a Rabi process.

Extrapolating these results into the regime of frequencies lower than shown in Fig. 6, the resonance peaks become very dense with respect to the frequency axis. This is due to the fact that the positions of neighboring resonances, which differ in the number of absorbed photons by 1, will differ only by the small photon energy corresponding to the low laser frequencies. The Rabi frequencies of the resonances will decrease for the increasing number of photons needed to create a pair; see Ref. [21]. Hence, only the very beginning of the Rabi oscillations and thus a quadratic time dependence of the average occupation number for a created pair with sharp momentum at a specific resonance will be observable. Incorporating the finite resolution of measuring the momenta of the produced pairs and the corresponding integration in momentum space (analogous to Fermi's golden rule), we expect that this leads to a

linear time dependence, i. e., a rate for pair production, which is characteristic for low laser frequencies in the tunneling regime.

#### 5.4. Polarization dependence of the resonance spectra

Going one step further, the resonance structure in Fig. 6 can also be calculated for different polarizations than  $\alpha_+ = \alpha_- = \pi/4$ . Performing a two-dimensional sweep over the laser frequency  $\omega$  and the polarization parameters  $\alpha_+$  and  $\alpha_-$  leads to the two-dimensional color plots shown in Fig. 8. The polarization parameters  $\alpha_+$  and  $\alpha_-$  are not varied independently; instead they either fulfill  $\alpha_+ = \alpha_-$  (corotating fields) or  $\alpha_- = \pi/2 - \alpha_+$  (antirotating fields).

Figure 8 shows the spin resolved electron creation probability for electrons with zero final momentum as a function of the laser frequency  $\omega$  and the polarization. The two plots on the left correspond to the spin-up and spin-down spectra for corotating fields, while the single plot on the right presents the spectrum for antirotating fields. Our numerical results show that the spectra depend on the spin orientation for corotating and are identical for both spin orientations in case of anti-rotating fields. Because spin-down and spin-up spectra are different for corotating fields, see left part of Fig. 8, it is possible to have for some fixed  $\omega$  and  $\alpha_+$  zero electron creation probability for a specific spin orientation and nonzero probability for the opposite orientation. For antirotating fields, however, the electron creation probability is completely symmetric with respect to the spin orientation of the created electron as shown in the right part of Fig. 8. Note that pair creation is suppressed for  $\alpha_+ = 0$  and  $\alpha_+ = \pi/2$ , i. e., circular polarization, in the case of corotating fields. For antirotating fields, however, resonances exist also for  $\alpha_+ = 0$  and  $\alpha_+ = \pi/2$ .

A possible interpretation of the different behavior of corotat-

ing and antirotating fields is that the standing electromagnetic wave carries nonzero spin density for corotating fields but not for antirotating fields. The orientation of the photonic spin density breaks the symmetry with respect to reflection along the propagation axis of the laser fields; see Fig. 2. Consequently, pair creation probabilities depend on the spin orientation of the created electrons. Note that for  $\alpha_+ = \pi/4$  (linear polarization) the photonic spin density vanishes also for corotating fields. Consequently, there is no dependence on the electron spin; see left part of Fig. 8. Pair creation probability becomes spin dependent, however, if  $\alpha_+ \neq \pi/4$ .

The parameter  $\alpha_+$  is restricted to the range from 0 to  $\pi/2$  in Fig. 8. One can show by the symmetry properties of the standing electromagnetic wave's vector potential (or its electromagnetic field) that for  $\alpha_+ = \alpha_-$  the spectra in Fig. 8 must be periodic in  $\alpha_+$  with period  $\pi$ . The part of the spectrum for  $\pi/2 \leq \alpha_+ \leq \pi$ , which is not shown in Fig. 8, can be obtained by mirroring the spectrum for  $0 \leq \alpha_+ \leq \pi/2$  at  $\alpha_+ = \pi/2$ . Furthermore, the spectrum is periodic in  $\alpha_+$  with period  $\pi/2$  for antirotating fields.

Figure 8 reveals an explicit spin dependence of the resonance structures in case of corotating fields. These differences become more pronounced the more the fields' ellipticity differs from linear polarization at  $\alpha_+ = \pi/4$ . The spectra for spin up, if mirrored along the line  $\alpha_+ = \pi/4$ , are equal to the spectra for spin down and vice versa. This can be understood by symmetry, because flipping the spin of the final particle leads to the same result as flipping the sense of rotation for the lasers' polarization, i. e., from right circulating polarization to left circulating polarization. Looking at the resonance between  $0.8 m_0 < \omega < 0.9 m_0$ , for example, the resonance frequency  $\omega_R$  decreases toward circular right polarization  $\alpha_+ \rightarrow \pi/2$  for spin up, while it increases for spin down.

Note that this shift of the resonance frequency is always opposite for electrons with spin up and with spin down. This might be understood by the coupling between the particle's spin and the lasers' magnetic field, as seen in the rest frame of the particle. With the electric and magnetic field components  $\mathbf{E}$  and  $\mathbf{B}$  in the laboratory frame, the magnetic field in the rest frame is in leading order  $\mathbf{B}' \sim \mathbf{B} - \mathbf{v} \times \mathbf{E}$ . Because  $\mathbf{B}$  is always perpendicular to the  $z$  axis, the Zeeman energy  $-q/(2m_0) \boldsymbol{\sigma} \cdot \mathbf{B}' = q/(2m_0) \boldsymbol{\sigma} \cdot (\mathbf{v} \times \mathbf{E})$  results, where  $\mathbf{v}$  denotes the particle's velocity in the laboratory frame. For corotating laser fields with elliptical polarization, the electric field rotates in the  $x$ - $y$  plane and therefore leads to a two-dimensional trajectory of the particle in the  $x$ - $y$  plane. Because  $\mathbf{E}$  also lies in the  $x$ - $y$  plane, the magnetic field  $\mathbf{v} \times \mathbf{E}$  points in the  $z$  direction yielding a modification of the particle's energy and in this way modifying the resonance frequency  $\omega_R$ . The sign of this energy shift depends on the particle's spin in the  $z$  direction, which explains the opposite shift of the resonance frequency for different spin orientations. For antirotating fields, in contrast, the electric field does not rotate in the  $x$ - $y$  plane. It oscillates with a fixed direction in the  $x$ - $y$  plane. Consequently, the particle's trajectory projected onto the  $x$ - $y$  plane will always be parallel to the electric field direction. Thus, the Zeeman energy is zero for an electron with spin in  $z$  direction, and consequently there is no spin-dependent shift of the resonance frequency.

The shift of the Zeeman energy, which we find in the case of corotating fields, is also given by the nonrelativistic corrections to the Pauli equation. These correction can be obtained by an expansion of the Dirac equation via a Foldy–Wouthuysen transformation and contains the term  $1/(4m_0^2) \boldsymbol{\sigma} \cdot (\mathbf{E} \times (-i\nabla - q\mathbf{A}))$ . For zero canonical momentum, this is up to a factor of 2 equivalent to the shift of the Zeeman energy discussed above. Note that the factor  $\mathbf{E} \times \mathbf{A}$  can be attributed to the photonic spin density of the electromagnetic field [34], which is zero for antirotating fields.

## 5.5. Comparison to the dipole approximation

When pair creation in standing electromagnetic waves is studied, neglecting the magnetic field component and the spatial variation of the electric field is a commonly applied approximation [31, 48, 49]. Therefore, we will analyze the effect of this approximation in this subsection. Neglecting the spatial variation of the electromagnetic field given by the potential (4) yields the dipole approximation vector potential

$$\mathbf{A}_{\pm}(t) = \text{Re} \left( \frac{\mathbf{E}}{i\omega} \left( \cos \alpha_{\pm} |l\rangle + \sin \alpha_{\pm} e^{i\varphi_{\pm}} |r\rangle \right) e^{-i\omega t} \right). \quad (41)$$

This dipole approximation of the electromagnetic fields is employed in Fig. 9 for comparison with Fig. 8, where the full electromagnetic field was taken into account. Also in the framework of the dipole approximation, Rabi oscillations of the electron creation probability and resonances can be found. The dipole approximation gives, however, results, which differ quantitatively as well as qualitatively from the case of pair creation in electromagnetic fields. For example, the number of resonances is reduced in case of the dipole approximation. In Fig. 9 the parameter  $\alpha_+$  ranges from 0 to  $\pi$  in order to point at differences to the simulation with the full monochromatic field and to show some peculiarities of the turn on and off of the electromagnetic field.

In case of corotating fields, the two plots on the left of Fig. 9 are not perfectly symmetric with respect to the line  $\alpha_+ = \pi/2$ , especially for  $0.9 m_0 \lesssim \omega \lesssim 1.2 m_0$ . This is due to the turn on and turn off as the following argument illustrates. Comparing, for example,  $\alpha_+ = \alpha_- = \pi/4$  with  $\alpha_+ = \alpha_- = 3\pi/4$ , both laser fields are linearly polarized with the electric field component pointing in the  $x$  direction and in the  $y$  direction, respectively. Due to rotational invariance around the  $z$  axis, both parameters should yield the same results. But owing to the parametrization and analytical structure of the vector potential (41), the electric field amplitude is at maximum for  $\alpha_+ = \alpha_- = \pi/4$  at  $t = 0$ , while it is zero for  $\alpha_+ = \alpha_- = 3\pi/4$  at  $t = 0$  maximal. This phase shift leads in combination with the window function (29) to an asymmetry, which has no effect in regimes with Rabi frequencies much slower than the laser frequency, because the pair production effect builds up over many laser cycles and is less sensitive to the initial phase of the laser field. For Rabi frequencies on the order of the laser frequency as observed for  $\omega \gtrsim m_0$  this difference, however, becomes noticeable.



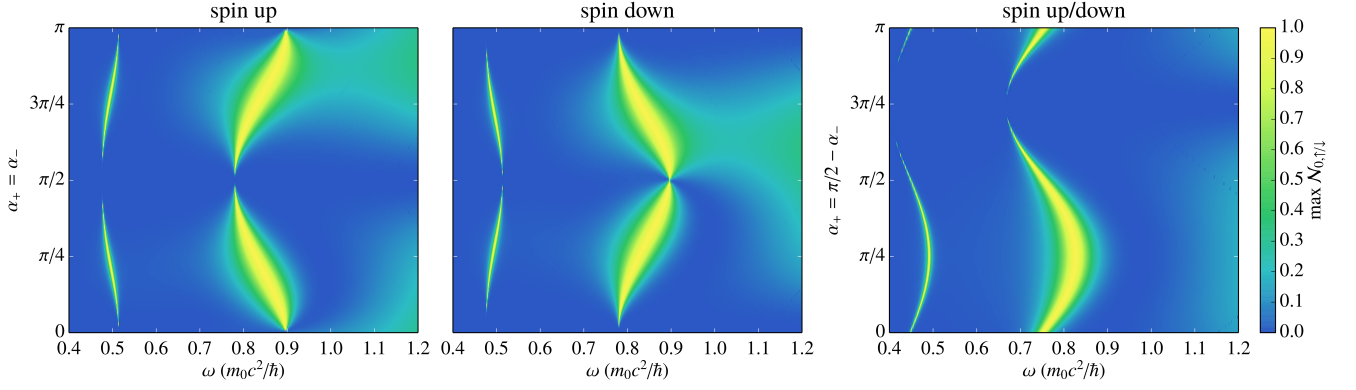


**FIG. 9:** (color online) Polarization and laser frequency dependence of the electron creation probability with zero final momentum and specific spin orientation with respect to the positive  $z$  direction when the dipole approximation is applied. All parameters as in Fig. 8.

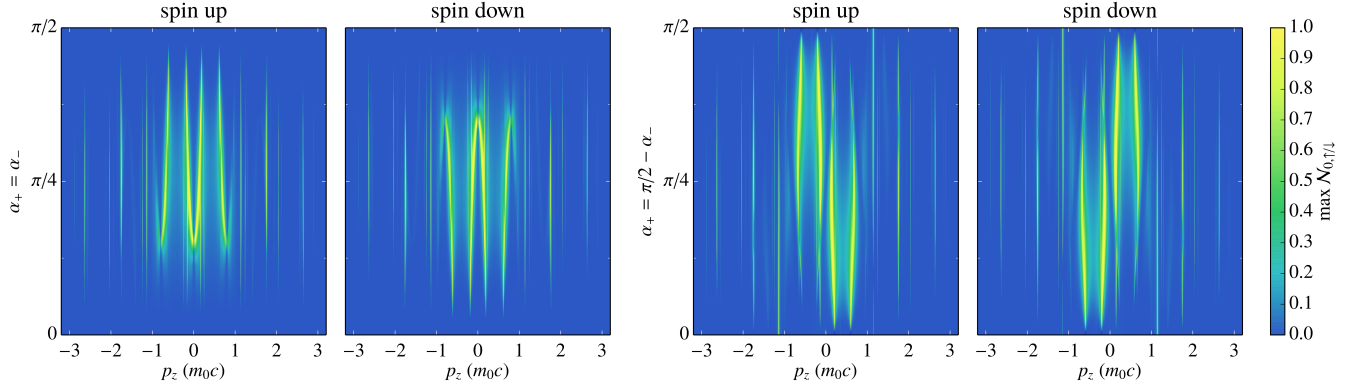


**FIG. 10:** (color online) Polarization dependence of the pair creation probability, where the electron has different final momenta  $\mathbf{p}_0 = (0, 0, p_z)$ . The lasers' frequencies are set to  $\omega = 0.8 m_0$ , and their strength is implicitly determined by  $\xi = 1/2$ . From all four plots can be inferred that, for this fixed frequency and strength, final pairs with distinguished momenta will be produced. Left two plots: These two plots correspond to the corotating field setup and differ by the spin orientation of the final electron. The vertical cut along  $p_z = 0$  corresponds to a vertical cut along  $\omega = 0.8 m_0$  in Fig. 8. Both plots are symmetric around  $p_z = 0$ . This is because inverting  $p_z$  would also invert the final helicity of the created particles, but due to the fact that for corotating fields both fields' helicities are opposite to each other, the systems stays invariant. Right two plots: These two plots correspond to the antirotating field setup. In contrast to the case of corotating fields, the spectra are not invariant under inversion of the  $p_z$  momentum and consequently the helicity of the final particle, because both laser fields have the same helicity for this case. But if, in addition to the momentum inversion, also the spin is inverted, the helicity of the final particle does not change, and the spectrum stays the same.

For the case of antirotating electromagnetic fields, we found in Sec. 5.4 that the probability to create an electron with zero momentum is periodic in the field parameter  $\alpha_+$  with period  $\pi/2$ . Applying the dipole approximation, however, the spectrum becomes periodic in  $\alpha_+$  with period  $\pi$  as shown in the right part of Fig. 9. This is a direct consequence of the symmetry properties of the vector potentials in (41). For  $\alpha_+ = \pi/4$  there are broad resonances, whereas pair creation is inhibited for  $\alpha_+ = 3\pi/4$ . Both parameters correspond to electric fields with linear polarization. For  $\alpha_+ = \pi/4$  the vector potentials  $\mathbf{A}_+(t)$  and  $\mathbf{A}_-(t)$  given in (41) superimpose constructively, while both potentials cancel for  $\alpha_+ = 3\pi/4$ . Note that this cancellation is a peculiarity of the dipole approximation. Two counterpropagating electromagnetic waves with temporal and spatial variation as specified in (4) cannot interfere such that both annihilate each other completely.

Notably, the simulation for the dipole approximation also yields a strong dependence of the pair creation on the spin of

the created electron and the polarization of the electric field for corotating fields while not for antirotating fields. Comparing the magnitude of the shift of the resonance frequency  $\omega_R$  with the one in Fig. 8 shows that this effect is even stronger in the dipole approximation with a rotating electric field only. As mentioned in the previous subsection, this shift might be due to the coupling of the particles spin and the magnetic field, as seen in the rest frame of the particle. Alternatively, the spin dependence could also be inferred from symmetry. In case of corotating electric fields, the sense of rotation changes under reflection of the  $z$  axis, and thus the pair creation probability might become spin dependent. In contrast, two antirotating electric fields form an electric field with a constant direction, and therefore the field configuration is symmetric under reflection of the  $z$  axis. Consequently, also pair creation is symmetric under reflection of the final particle's spin, assuming zero final momentum.

Comparing the various resonances in Figs. 8 and 9 in terms

of the polarization dependent shift of the resonance frequencies shows that the frequency shift becomes smaller at lower laser frequencies. The reason for this might be a combination of the decreased amount of photon energy and an averaging effect due to the increased number of photons. The polarization dependence of the resonance frequencies tends to be larger for the dipole approximation than for the case of electromagnetic fields, which may be attributed to the fact that the electric field is maximal at each point in space within the dipole approximation and to the absence of the magnetic field in the laboratory frame.

## 5.6. Final momentum dependence of the resonance spectra

In the previous subsections, we investigated the creation of particles with zero final momentum. Looking, for example, at Fig. 8, it shows that at  $\omega \sim 0.8 m_0$  no particles with zero final momentum can be created for the given setup. Particles with nonvanishing momentum, however, might be created. A sweep over the final momentum allows us to study the momentum dependence of the pair production probability. Due to the fact, that a three-dimensional sweep over all final momenta is numerically quite expensive and also hard to visualize, we vary only the momentum directed along the  $z$  axis, i. e., the lasers' propagation axis. The perpendicular momenta are set to zero. Furthermore, we chose a fixed laser frequency of  $\omega = 0.8 m_0$  and additionally scanned over the ellipticity for corotating and antirotating field configurations as done in Figs. 8 and 9. The numerical result is shown in Fig. 10. The two plots on the left correspond to corotating fields, while the two on the right correspond to antirotating fields. In agreement with our previous calculations, Fig. 10 indicates that no particles are created with zero final momentum for the fixed frequency of  $\omega = 0.8 m_0$ . Pair creation is possible for some nonvanishing momenta as the resonances in Fig. 10 indicate. A notable peculiarity for the case of corotating fields can be seen in the left part of Fig. 10. Tracing the two broader resonances close to  $p_z = 0$  for the spin up case from top to bottom, they approach each other but do not join each other at  $p_z = 0$  for  $\alpha_+ \sim \pi/8$ . Thus, pair creation is suppressed at  $p_z = 0$  exactly consistent with Fig. 8.

These resonances in Fig. 10 exhibit distinctive symmetries. For corotating fields, both plots for spin up and spin down are symmetric around the line  $p_z = 0$ . This symmetry is related to the fact that inverting the  $z$  momentum preserves the relative orientation of the helicities of the created electron and the two counterpropagating waves. Inverting the final momentum inverts the helicity of the electron. Because both laser fields' helicities are opposite to each other for corotating fields, inverting the  $z$  momentum or equally the helicity of the created electron does not change the system. The electron's helicity is parallel to one wave and antiparallel to the other as before inversion of the  $z$  momentum.

Both helicities of the laser fields point into one preferred direction for antirotating fields. Thus, inverting the  $z$  momentum does not leave the system invariant, and electrons are created preferably with helicity parallel or antiparallel to the helicity of

the electromagnetic fields. To preserve the relative orientation of the helicities of the created electron and the two counterpropagating waves, one has to invert the  $z$  momentum and the waves' helicity, which corresponds to the combined transformation  $p_z \rightarrow p_z$  and  $\alpha_+ \rightarrow \pi/2 - \alpha_+$ , and thus the spectra in the right part of Fig. 10 are invariant under this transformation.

Both the corotating as well as the antirotating case have in common that mirroring the spectrum for one spin orientation around the  $\alpha_+ = \pi/4$  line yields the spectrum for the other spin orientation. This symmetry holds for the spectra in Fig. 8 as well as in Fig. 10. Again, this is a consequence of the system's invariance under flipping the created electron's spin/helicity and the field's spin/helicity.

Let us compare the spectra for corotating fields with the ones for antirotating fields in Fig. 10 at fixed values of the ellipticity parameter  $\alpha_+$ . In the case of corotating fields, electrons with spin up or down are created with higher probability depending on the ellipticity parameter  $\alpha_+$ ; see the left part of Fig. 10. Because of the symmetry properties described in detail above, the electrons are created with equal probability having positive or negative helicity; this means created electrons propagate in the positive or negative  $z$  direction with equal probability. This changes if we consider antirotating fields; see the right part of Fig. 10. Here electron creation is spin symmetric. This means spin-up and spin-down electrons are created with equal probability. However, electrons with positive or negative helicity are created with higher probability depending on the ellipticity parameter  $\alpha_+$ . For an ellipticity of  $\alpha_+ \sim \pi/8$ , for example, electrons are created preferably with spin up, which propagate only along the positive  $z$  direction, and with spin down, which propagate only along the negative  $z$  direction.

## 6. Conclusions

We studied pair creation in strong electromagnetic fields in the nonperturbative regime, i. e.,  $\xi \sim 1$ . For this purpose, we derived a numerical framework for solving the time-dependent Dirac equation for an electron in two counterpropagating monochromatic laser fields with equal frequency. This setup is quite generic, because also other setups with two lasers having unequal frequencies or a colliding angle different than  $180^\circ$  could be incorporated by a proper Lorentz transformation. Furthermore, the polarization and the field strength of each individual laser field could be chosen arbitrarily. With this we overcame the so often applied dipole approximation for the laser fields and included the electric field's space dependence as well as the magnetic field's influence on pair production, leading to true three-dimensional dynamics. For numerical feasibility and in order to keep the space of possible parameters small, high laser frequencies and equal intensity and polarization of the counterpropagating fields were assumed. The numerical method, however, is also capable of treating setups with unequal polarizations and intensities. It can be easily generalized to multicolor setups, provided that all frequencies are low-order harmonics of some base frequency.

It was shown that switching off the external laser fields is

essential for a proper determination of the pair creation probabilities. These probabilities exhibit the characteristic features of Rabi oscillations with the corresponding resonance frequencies and Rabi frequencies. The resonance structures and their dependencies on the final quantum numbers of the produced pairs as well as on the polarization of the laser field were investigated numerically in more detail.

A quite remarkable result is the observation that, by tuning the polarization of the two laser beams, spin polarized pairs can be created. By using corotating laser fields, for example, the

spins of the electrons in the produced pairs may be aligned all the same along the propagation axis of the lasers. Antirrotating fields, in contrast, may yield electrons with spin-up propagating forward and electrons with spin down propagating backward with respect to the lasers' propagation axis.

## Acknowledgments

We are thankful for stimulating discussions with S. Ahrens and C. Müller at the onset of this work.

- 
- [1] F. Sauter, *Z. Phys.* **69**, 742 (1931).
  - [2] W. Heisenberg and H. Euler, *Z. Phys.* **98**, 714 (1936).
  - [3] J. Schwinger, *Phys. Rev.* **82**, 664 (1951).
  - [4] F. Ehlotzky, K. Krajewska, and J. Z. Kamiński, *Rep. Prog. Phys.* **72**, 046401 (2009).
  - [5] A. Di Piazza, C. Müller, K. Z. Hatsagortsyan, and C. H. Keitel, *Rev. Mod. Phys.* **84**, 1177 (2012).
  - [6] M. Altarelli, R. Brinkmann, M. Chergui, W. Decking, B. Dobson, S. Düsterer, G. Grübel, W. Graeff, H. Graafsma, J. Hajdu, J. Marangos, J. Pflüger, H. Redlin, D. Riley, I. Robinson, J. Rossbach, A. Schwarz, K. Tiedtke, T. Tschentscher, I. Vartanants, H. Wabnitz, H. Weise, R. Wichmann, K. Witte, A. Wolf, M. Wulff, and M. Yurkov, eds., *The European X-Ray Free-Electron Laser Technical Design Report* (DESY XFEL Project Group European XFEL Project Team Deutsches Elektronen-Synchrotron Member of the Helmholtz Association, Hamburg, 2007).
  - [7] V. Yanovsky, V. Chvykov, G. Kalinchenko, P. Rousseau, T. Planckon, T. Matsuoka, A. Maksimchuk, J. Nees, G. Cheriaux, G. Mourou, and K. Krushelnick, *Opt. Express* **16**, 2109 (2008).
  - [8] B. W. J. McNeil and N. R. Thompson, *Nat. Photonics* **4**, 814 (2010).
  - [9] P. Emma, R. Akre, J. Arthur, R. Bionta, C. Bostedt, J. Bozek, A. Brachmann, P. Bucksbaum, R. Coffee, F.-J. Decker, Y. Ding, D. Dowell, S. Edstrom, A. Fisher, J. Frisch, S. Gilevich, J. Hastings, G. Hays, P. Hering, Z. Huang, R. Iverson, H. Loos, M. Messerschmidt, A. Miahnahri, S. Moeller, H.-D. Nuhn, G. Pile, D. Ratner, J. Rzepiela, D. Schultz, T. Smith, P. Stefan, H. Tompkins, J. Turner, J. Welch, W. White, J. Wu, G. Yocky, and J. Galayda, *Nat. Photonics* **4**, 641 (2010).
  - [10] G. A. Mourou, N. J. Fisch, V. M. Malkin, Z. Toroker, E. A. Khazanov, A. M. Sergeev, T. Tajima, and B. Le Garrec, *Opt. Commun.* **285**, 720 (2012).
  - [11] A. Ringwald, *Phys. Lett. B* **510**, 107 (2001).
  - [12] R. Alkofer, M. B. Hecht, C. D. Roberts, S. M. Schmidt, and D. V. Vinnik, *Phys. Rev. Lett.* **87**, 193902 (2001).
  - [13] D. B. Blaschke, A. V. Prozorkevich, C. D. Roberts, S. M. Schmidt, and S. A. Smolyansky, *Phys. Rev. Lett.* **96**, 140402 (2006).
  - [14] A. R. Bell and J. G. Kirk, *Phys. Rev. Lett.* **101**, 200403 (2008).
  - [15] D. B. Blaschke, A. V. Prozorkevich, G. Röpke, C. D. Roberts, S. M. Schmidt, D. S. Shkirmanov, and S. A. Smolyansky, *Eur. Phys. J. D* **55**, 341 (2009).
  - [16] E. Brezin and C. Itzykson, *Phys. Rev. D* **2**, 1191 (1970).
  - [17] V. S. Popov, *JETP Letters* **13**, 185 (1971).
  - [18] C. D. Roberts, S. M. Schmidt, and D. V. Vinnik, *Phys. Rev. Lett.* **89**, 153901 (2002).
  - [19] F. Hebenstreit, R. Alkofer, G. V. Dunne, and H. Gies, *Phys. Rev. Lett.* **102**, 150404 (2009).
  - [20] C. K. Dumlu and G. V. Dunne, *Phys. Rev. Lett.* **104**, 250402 (2010).
  - [21] G. R. Mocken, M. Ruf, C. Müller, and C. H. Keitel, *Phys. Rev. A* **81**, 022122 (2010).
  - [22] M. Orthaber, F. Hebenstreit, and R. Alkofer, *Phys. Lett. B* **698**, 80 (2011).
  - [23] A. Nikishov, *Nucl. Phys. B* **21**, 346 (1970).
  - [24] H. Gies and K. Klingmüller, *Phys. Rev. D* **72**, 065001 (2005).
  - [25] G. V. Dunne and Q.-h. Wang, *Phys. Rev. D* **74**, 065015 (2006).
  - [26] S. P. Kim and D. N. Page, *Phys. Rev. D* **75**, 045013 (2007).
  - [27] H. Kleinert, R. Ruffini, and S.-S. Xue, *Phys. Rev. D* **78**, 025011 (2008).
  - [28] M. Ruf, G. R. Mocken, C. Müller, K. Z. Hatsagortsyan, and C. H. Keitel, *Phys. Rev. Lett.* **102**, 080402 (2009).
  - [29] S. S. Bulanov, V. D. Mur, N. B. Narozhny, J. Nees, and V. S. Popov, *Phys. Rev. Lett.* **104**, 220404 (2010).
  - [30] F. Hebenstreit, R. Alkofer, and H. Gies, *Phys. Rev. Lett.* **107**, 180403 (2011).
  - [31] Z. L. Li, D. Lu, B. F. Shen, L. B. Fu, J. Liu, and B. S. Xie, "Mass shift effects in nonperturbative multiphoton pair production for arbitrary polarized electric fields," (2014), arXiv:1410.6284.
  - [32] Q. Su, W. Su, Q. Z. Lv, M. Jiang, X. Lu, Z. M. Sheng, and R. Grobe, *Phys. Rev. Lett.* **109**, 253202 (2012).
  - [33] A. Wöllert, M. Klaiber, H. Bauke, and C. H. Keitel, *Phys. Rev. D* **91**, 065022 (2015).
  - [34] H. Bauke, S. Ahrens, C. H. Keitel, and R. Grobe, *New J. Phys.* **16**, 103028 (2014).
  - [35] T.-O. Müller and C. Müller, *Phys. Rev. A* **86**, 022109 (2012).
  - [36] C. Müller, H. Hu, B. Najjari, J. R. Crespo López-Urrutia, Z. Harman, and A. B. Voitkiv, *Journal of Physics: Conference Series* **388**, 012003 (2012).
  - [37] R. C. Jones, *J. Opt. Soc. Am.* **31**, 488 (1941).
  - [38] K. Y. Bliokh, A. Y. Bekshaev, and F. Nori, *New J. Phys.* **15**, 033026 (2013).
  - [39] E. S. Fradkin, D. M. Guitman, and S. M. Shvartsman, *Quantum Electrodynamics with Unstable Vacuum*, Springer Series in Nuclear and Particle Physics (Springer, Berlin, 1991).
  - [40] F. Gross, *Relativistic Quantum Mechanics and Field Theory* (Wiley-VCH, Weinheim, 2004).
  - [41] B. Thaller, *Advanced Visual Quantum Mechanics* (Springer, Heidelberg, 2005).
  - [42] In general the function sets  $\pm\varphi_n(\mathbf{r})$  and  $\pm\varphi_n(\mathbf{r})$  may not coincide because the vector potential may not vanish and be different at  $t_{\text{in}}$  and  $t_{\text{out}}$ , depending on the gauge.

- [43] D. M. Gitman, *J. Phys. A: Math. Gen.* **10**, 2007 (1977).
- [44] H. Bauke and C. H. Keitel, *Comput. Phys. Commun.* **182**, 2454 (2011).
- [45] Due to the fact that the propagation is back in time, the mentioned “turn on” really corresponds to the turn-off, as the propagation starts at the end of the laser field. However, a positive time flow seems more natural for the discussion of the numerical results and therefore we stick to the labeling “turn on”.
- [46] S. Ahrens, H. Bauke, C. H. Keitel, and C. Müller, *Phys. Rev. Lett.* **109**, 043601 (2012).
- [47] S. Ahrens, H. Bauke, C. H. Keitel, and C. Müller, *Phys. Rev. A* **88**, 012115 (2013).
- [48] A. M. Fedotov, E. G. Gelfer, K. Y. Korolev, and S. A. Smolyan-sky, *Phys. Rev. D* **83**, 025011 (2011).
- [49] A. Blinne and H. Gies, *Phys. Rev. D* **89**, 085001 (2014).